scientific reports

OPEN

# A functional digital model of the Dingo thermal neutron imaging beamline

Klaudiusz Jakubowski[1,2], Joseph J. Bevitt[1], Nicholas Howell[1], Chris Dobie[1], Frederic Sierro[1], Ulf Garbe[1], Scott Olsen[1], Attila Stopic[1], Daniel R. Franklin[3], Linh T. Tran[2], Anatoly Rosenfeld[2], Susanna Guatelli[2] & Mitra Safavi-Naeini[1,2]✉

**In this work, we extend our previously published Monte Carlo simulation model of the Dingo thermal neutron beamline at the Australian Centre for Neutron Scattering model by (1) including a sapphire crystal filter in the model, and (2) utilising the NCrystal package to simulate thermal neutron interactions with the crystalline structure. In addition to previous experimental measurements performed in the beamline's high-resolution mode, the beam was experimentally characterised in its high-intensity mode upstream from the sample stage (at the tertiary shutter wall exit) and these measurements were used as inputs for the model. The planar neutron distributions were optimised at both the sample stage and tertiary shutter wall exit, and model predictions were validated against experimental gold wire activation measurements. For both configurations—with and without the sapphire filter—we measured neutron fluxes, and performed neutron activation analysis using 11 materials to improve the accuracy of the neutron spectrum in the model relative to the original version. Using the optimised spectrum, we simulated out-of-beam neutron spectra that were further used as the initial input in unfolding code to explore the capability of the current solution to accurately reproduce the experimental results. The normalised neutron planar distribution from the simulation was on average within 2% at the centre, and 6% and 24% at the penumbra of the experimental results at the tertiary shutter wall exit and sample stage, respectively. The specific activities predicted by the refined model were within an average of 13% and 5% of the experimentally measured activities with and without the sapphire filter, respectively. We observed a decrease of around 45% in thermal neutron flux when the sapphire filter is used, which has been reproduced by the model. The maximum value of the logarithm of the ratio of simulated to experimental out-of-beam neutron spectra across 8 locations was 0.6 compared to 2.0 in the previous work, resulting in an average normalised root mean squared error between the unfolded spectrum and experimental measurements of 5% and 9% with and without the filter, respectively. Without the sapphire filter, the optimised predicted in-beam neutron spectrum consists of around 59% thermal, 21% epithermal and 20% fast neutrons, while the addition of the filter provides an almost pure (approximately 98%) thermal neutron beam.**

The Australian Centre for Neutron Scattering (ACNS) Dingo high-flux thermal neutron beamline is a versatile instrument primarily used for neutron radiography and tomography[1,2]. While nominally a thermal neutron beamline, the beam delivers epithermal and fast neutron components as well as a gamma component. For applications requiring a specific energy distribution, the spectrum of the Dingo beam can be modified using cadmium and sapphire filters.

Cadmium, a well-known thermal neutron absorber, contains $^{113}$Cd (12.22% abundance in natural cadmium) with a thermal neutron capture cross-section of $\approx 20{,}000$ barns, dropping sharply at $\approx 0.55$ eV. Sapphire crystal (corundum, $\mathrm{Al_2O_3}$) effectively filters neutrons below and above the thermal energy range. Neutron transmission through the crystal depends on its thickness, cut axis (*a* or *c*), quality, perfection, operating temperature and mosaicity (spread of crystal plane orientations). Neutron transmission below $\mathrm{E}_n < 0.02$ eV can increase by $\approx 5$ to 18% when cooled to $\approx 100$ K, though this modest improvement rarely justifies the added cost and complexity[3]. High-quality single crystals cut along the *a*-axis feature more parasitic Bragg reflections from the

[1]Australian Nuclear Science and Technology Organisation (ANSTO), Lucas Heights, NSW 2234, Australia. [2]Centre for Medical Radiation Physics, University of Wollongong, Wollongong, NSW 2522, Australia. [3]School of Electrical and Data Engineering, University of Technology Sydney, Sydney, NSW 2007, Australia. ✉email: mitras@ansto.gov.au

(119) and (113) planes relative to cuts along the *c*-axis, causing more fluctuations in neutron transmission[4–6]. Therefore, *c*-axis cut crystals are preferred for neutron filtering applications.

In our previous work, we developed a detailed CAD-based Monte Carlo model of Dingo's complete beam transportation system and bunker shielding[7]. The planar distribution of the neutron beam was optimised using thermal and epithermal neutron fluence data measured with gold activation foils and $B_4C$-coated microdosimeters. We simulated the out-of-beam neutron spectra and validated the model's predictions against experimental Bonner sphere results placed in 8 locations parallel to the sample stage, iteratively selecting the best-performing solution to predict the neutron spectrum in-beam at the sample stage position.

Since our previous study, Dingo's sample room configuration has been modified. Notably, a sapphire filter has been added to eliminate most of the epithermal and fast components of the beam. Dingo can operate in either a high-resolution mode, with a $10\ \mathrm{cm}\ \times\ 10\ \mathrm{cm}$ field size at the sample stage, or a high-intensity mode, with a $20\ \mathrm{cm}\ \times\ 20\ \mathrm{cm}$ field size. Our previous work focused on the high-resolution mode. This study aims to experimentally characterise the $20\ \mathrm{cm}\ \times\ 20\ \mathrm{cm}$ high-intensity beam, optimise the simulation model parameters to match the observations, refine the previously predicted neutron spectrum, implement a sapphire filter and evaluate its performance, and develop a user-friendly simulation with a graphical user interface (GUI). The results of this work and the refined Monte Carlo model will form a core element of a platform for research and development of detectors for high-intensity mixed gamma/neutron fields and radiobiological research in Australia, such as the development of novel neutron capture agents for Neutron Capture Enhanced Particle Therapy (NCEPT) or Boron Neutron Capture Therapy (BNCT)[8–11].

The most common methods for absolute neutron spectrum measurements are Bonner sphere spectroscopy and neutron activation analysis (NAA). Both require unfolding of the neutron spectra and do not provide a unique solution[12,13]. Bonner sphere spectroscopy uses several high-density spherical polyethylene moderators of different thicknesses and a $^6$LiF or $^3$He detector, $^6$LiI scintillator, or a neutron activation material (e.g., gold) to measure neutron spectra. Unfolding requires a response matrix for each moderator and an initial guess spectrum, typically generated from Monte Carlo simulations (MNCPX, Geant4 or PHITS). Alternatively, the calculation can be initiated using a $1/E_n$ Maxwellian distribution.

In NAA, isotopes with high neutron capture cross-sections within specific energy windows are irradiated, forming excited states that decay to its ground state via the emission of characteristic $\gamma$-rays. Reactions can be non-threshold (exothermic) or threshold (endothermic), the latter predominant for fast neutrons above hundreds of keV. Ideal materials have a high abundance of the parent isotope, dominant $\gamma$ branching ratio, suitable photon energies for detection, and half-lives of the daughter isotopes between 1 h and a few days to achieve sufficient specific activity while minimising the dose to personnel.

In this paper, we characterise and optimise the dimensions and relative uniformity of the $20\ \mathrm{cm}\ \times\ 20\ \mathrm{cm}$ high-intensity beam in our simulation framework. This configuration is best suited for radiobiological research and is used most frequently for neutron tomography at Dingo. We measured the thermal neutron flux and spatial distribution, and performed NAA with a set of 11 materials, sensitive to either broad or narrow energy bands, to measure the neutron spectra directly in-beam at the tertiary shutter wall exit, both with and without the sapphire filter. This approach allows us to measure specific bins within the neutron energy spectrum, providing a more detailed characterisation of the beam. Using these NAA data, we refined the neutron spectrum in our model and re-simulated the full beamline. To validate the refined model, we then used it to predict out-of-beam neutron spectra and compared these predictions with experimental Bonner sphere measurements, using our simulated spectra as initial guesses in the unfolding algorithm for the Bonner sphere data. The validated model presented here provides a robust foundation for developing a fully functional digital twin, capable of incorporating real-time data synchronisation in future work.

The method for implementing the sapphire filter in the Monte Carlo model in Geant4 is explained in section "Implementation of the sapphire crystal filter". The absolute neutron flux measurements are described in sections "Absolute neutron flux measurements at the tertiary shutter wall exit", "Relative neutron planar distribution with gold activation wires" and "Absolute in-beam neutron activation analysis" define the approach to measure and validate the neutron planar distribution with gold activation wires, as well as the NAA of the experimental data and optimisation of the neutron spectrum in the model. Section "Absolute out-of-beam Bonner Sphere spectroscopy" details the methodology to evaluate the refined neutron spectrum's performance out of the beam. Sections "Results" and "Discussion" present the results of this work and the discussion. We summarise the study and list our conclusions in section "Conclusion".

## Materials and methods

All simulations were carried out using Geant4 (version 11.1, patch 1)[14–16]. The physics models used in this work are listed in Supplementary Materials Table S1. As in our previous work, we started with a 6 cm diameter circular beam to simulate the high-intensity mode. The beam travels along the *z* axis in the negative direction, with a $1.0^\circ$ (17.45 mrad) angular $\sigma_x$ and $\sigma_y$—the standard deviation in the beam directional profile. Inter-simulation variations were calculated using 95% confidence intervals. In this study, the thermal, epithermal and fast neutron energy bands are defined as $\mathrm{E}_{th} < 0.4\ \mathrm{eV}, 0.4\ \mathrm{eV} < \mathrm{E}_{epi} < 10\ \mathrm{keV}$ and $\mathrm{E}_{fast} > 10\ \mathrm{keV}$, respectively. All neutron spectra plotted in the results section are normalised 1) to the experimental neutron flux for both configurations (unfiltered and with the sapphire filter), 2) unit fluence, and 3) unit lethargy, where the latter is calculated as follows:

$$\Delta u = \log\left(\frac{E_{j+1}}{E_j}\right) \tag{1}$$

The Geant4 model of the Dingo beamline has been revised to allow for more flexibility in simulating either the complete beamline or selected zones; its structure is presented in Fig. 1. The pipeline applied in this work, which is explained in the following sections, is shown in Fig. 2. The new graphical user interface (GUI), developed in Python using ttk-inker, part of the Tkinter libraries for macro generation and simplified navigation through the command list and file browser, is illustrated in Fig. 3. The GUI provides user-friendly controls for setting simulation parameters, selecting beamline components (e.g., filters, collimators), and visualising neutron flux and energy spectra. It facilitates rapid iteration and optimisation of neutron beam simulations for various experimental scenarios.

## Implementation of the sapphire crystal filter

Further beam modification at Dingo is possible with the use of a sapphire crystal, which can remove up to around 95% of cold, epithermal and fast neutrons. The sapphire crystal installed at Dingo was supplied by Global Optics (UK) and consists of two $9 \text{ cm} \times 9 \text{ cm}$ stacks of five 3 cm thick high-quality sapphire crystals cut along the *c*-axis, each centred relative to the high-intensity or high-resolution beam. Sapphire crystals are held together by an aluminium housing, high-density polyethylene and the filter assembly attached to an $x$–$y$ motion stage. The transmission probability of a 15 cm thick sapphire crystal is shown in Fig. 4, where only high-quality crystals (sccutoff = 0.2A) with 1 arcmin mosaicity were plotted. Cooling down the crystal to 100K increases and broadens the crystal's transparency to thermal neutrons. Using a sapphire crystal cut along the *c*-axis allows us to narrow the transmission boundaries around 0.1-0.5 eV. There are alternative candidates for filtering thermal neutrons, such as liquid nitrogen-cooled silicon, quartz $SiO_2$ and bismuth. However, these are outperformed by sapphire crystals in distinguishing the thermal neutron component from fast neutrons, or softening the Maxwellian spectrum[17].

The thermal interactions of neutrons with the sapphire crystal in Geant4 are modelled using the NCrystal package, which is limited to the serial mode (single-core)[18,19]. Changing between multi-threaded and serial modes in Geant4 is possible with `G4RunManagerFactory`. Bragg diffraction was not included in the simulation model, while the available list of commands and crystal parameters can be found in[20]. The neutron spectrum in the model was iteratively adjusted until transmission through the crystal was within 10% of the experimental results. This was evaluated using a $1 \text{ cm} \times 1 \text{ cm}$ beam and a scoring plane of the same dimensions placed behind the sapphire crystal, or in the air. Neutron transmission in the experiment was estimated on the basis of the neutron flux with and without the sapphire filter measured with gold wires, which are sensitive to neutrons up to approximately 1 keV. In the simulation, neutrons with higher energies were filtered out and the

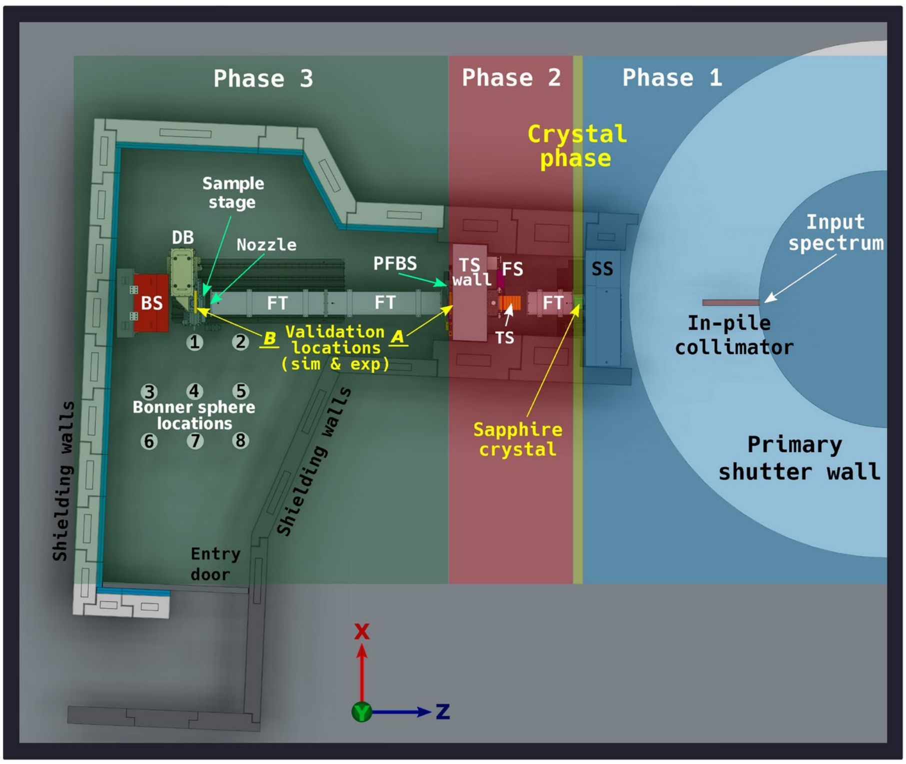


**Fig. 1**. Schematics of the ACNS Dingo beamline model showing simulation phases, experimental Bonner sphere locations, and scoring plane positions. SS—secondary shutter; FT—flight tubes; FS—fast neutron shutter; TS—tertiary shutter; PFBS—pre-flight tube beam slits; DB—detector box; and BS—beam stop. Shielding roof has been removed for improved visualisation. Measurement locations are indicated in yellow. Figure prepared using Autodesk Inventor 2022 (https://www.autodesk.com/products/inventor).

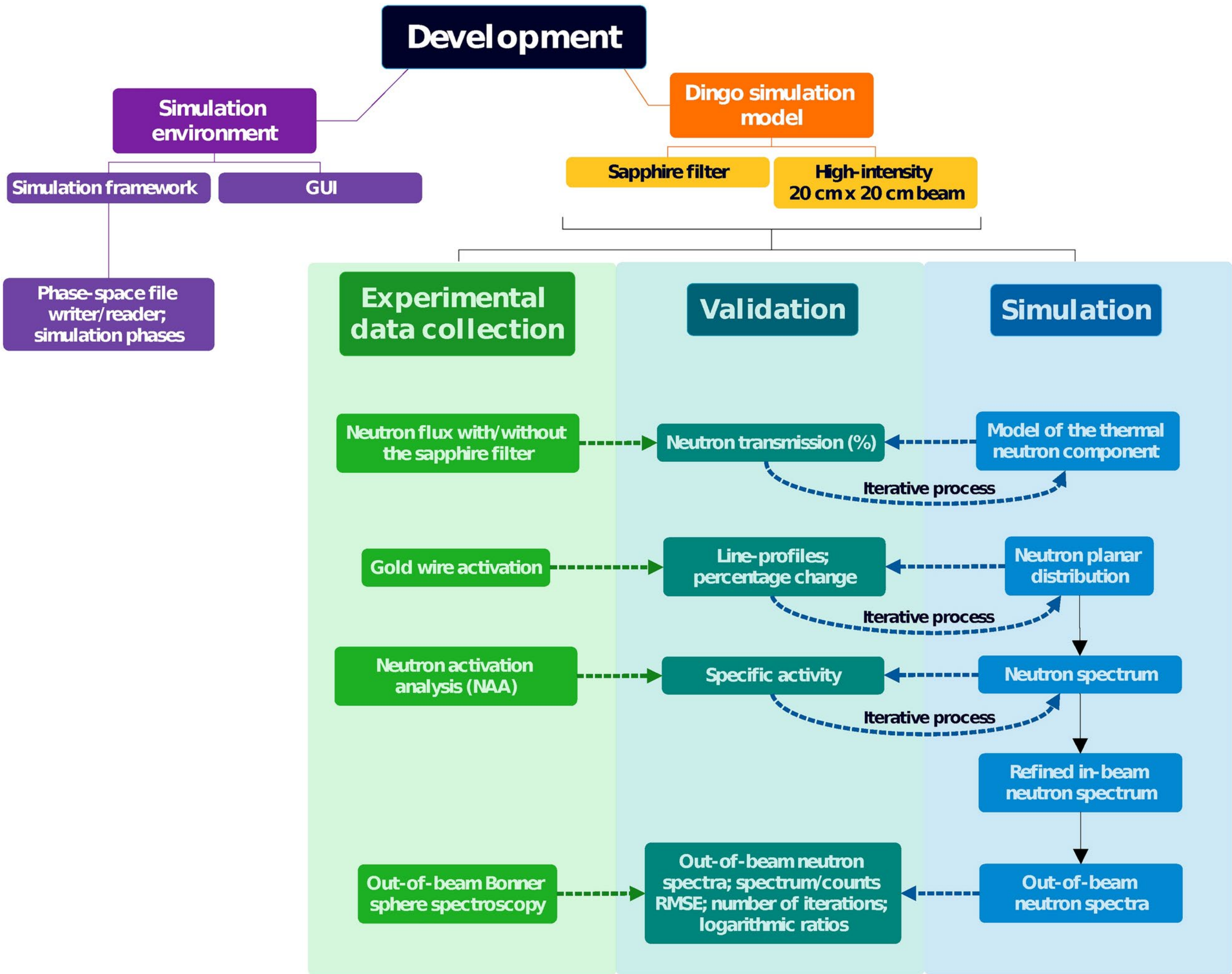


**Fig. 2**. Workflow diagram for developing a functional digital twin of the Dingo beamline, showing the integration of simulation development, experimental measurements, validation steps, and iterative refinement processes. Green boxes indicate experimental data collection, blue boxes show simulation components, and teal boxes represent the validation process.

percentage change in the neutron current for both configurations was calculated. Table 1 lists the parameters of the sapphire crystal used in the simulation model.

### Absolute neutron flux measurements at the tertiary shutter wall exit

In the first step of this work, we measured the absolute thermal and epithermal neutron flux using 0.25 mm diameter bare gold activation wires (approximately 1.5 cm long), and wires covered with a cadmium tube (12 cm long), as illustrated in Fig. 5. Cadmium tubes are of natural abundance and are 10 cm long with 1 mm internal diameter and 0.5 mm wall thickness. To estimate the relative centre of the beam, we attached a radiochromic film to the sample holder and irradiated it for 15 min. Radiochromic films (RCFs) are sensitive to $\gamma$ radiation produced within the beam transportation system. We attached the gold wires to the film and placed the sample holder at the tertiary shutter wall exit (location A), approximately 5 metres upstream of the sample stage. The samples were then irradiated using the high-intensity mode in two configurations—(1) with a sapphire filter in place for 15 h and 15 min; and (2) without the filter for 7 h and 35 min. After irradiation, around 5 cm of the gold wires covered with cadmium tubes were cut from the centre. Activation of the samples was measured with ORTEC's high-purity germanium (HPGe) detector. The calculated neutron flux was then used to normalise the NAA simulation results in the subsequent steps.

### Relative neutron planar distribution with gold activation wires

Next, we measured the neutron planar distribution at location A and sample stage (location B) using gold activation wires, that extended to the distal edges, penumbra and out-of-beam regions. This knowledge is crucial for radiography and tomography of larger samples, i.e., fossils and engineering samples; or radiobiological research using smaller samples or flasks that intend to be placed within the flat region at the centre of the field. We used 15 gold wires (1 cm long, 0.2 mm diameter) at location A and 27 at location B (1 cm long, 0.25 mm

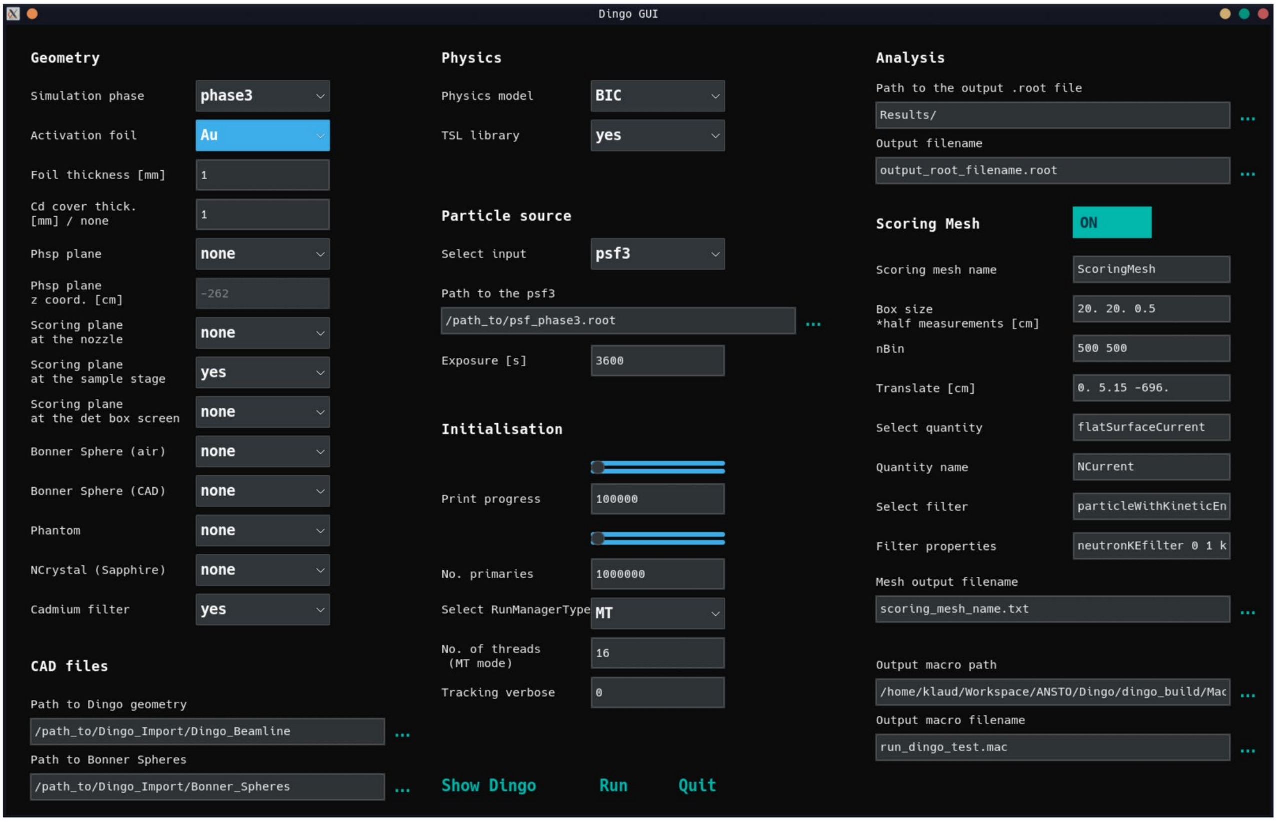


**Fig. 3**. The proposed Dingo graphical user interface (GUI) for simulation parameter configuration, sapphire filter implementation, beamline geometry visualisation, and output selection. The interface simplifies the simulation process for users unfamiliar with Geant4 and can initiate simulations on a local platform or generate macros with the selected parameters for use on a cluster.

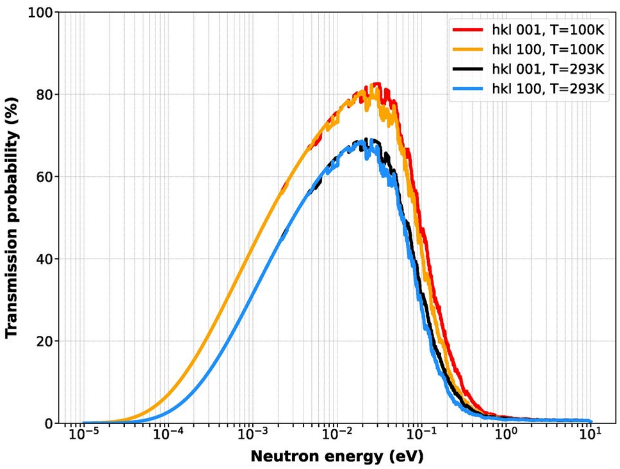


**Fig. 4**. Transmission probability through a 15 cm thick sapphire crystal at 100 K and 293 K for *a*- and *c*-axis orientations.

diameter). These were aligned with a 5 cm horizontal and 3 cm vertical step at both locations (see Fig. 6). The samples at the very top of location B were placed above the sample holder frame 4 cm from the next row to ensure their position out of beam. The gold wires were then irradiated for 7 h, and their activation was measured with a high-purity HPGe detector. In this step, we did not use cadmium-covered gold wires and so, the results are normalised to the maximum specific activity. In the simulation, we used $40\ \text{cm} \times 40\ cm$ scoring planes at both locations to record the neutron current passing through the voxels. The results were validated against the experimental specific activities by plotting line profiles along the $y$-axis of the beam, normalised in two

| Parameter (NCrystal variable) | Value |
|---|---|
| Formula | $Al_2O_3$ (Corundum) |
| Space group (sg) | 167 |
| Temperature (temp) | 293 K |
| Single crystal cut-off (sccutoff) | 0.2 |
| Mosaicity (mos) | 1 arcmin |
| Primary orientation axis (dir1) | 0 0 1 |
| Secondary orientation axis (dir2) | 0 1 0 |
| Secondary direction tolerance parameter (dirtol) | $180°$ |
| Bragg diffraction (bragg) | 0 |

**Table 1**. Specifications of the sapphire crystal used in the Dingo beamline model, including structural, thermal, and orientation parameters relevant for neutron transmission and filtering performance in simulation.

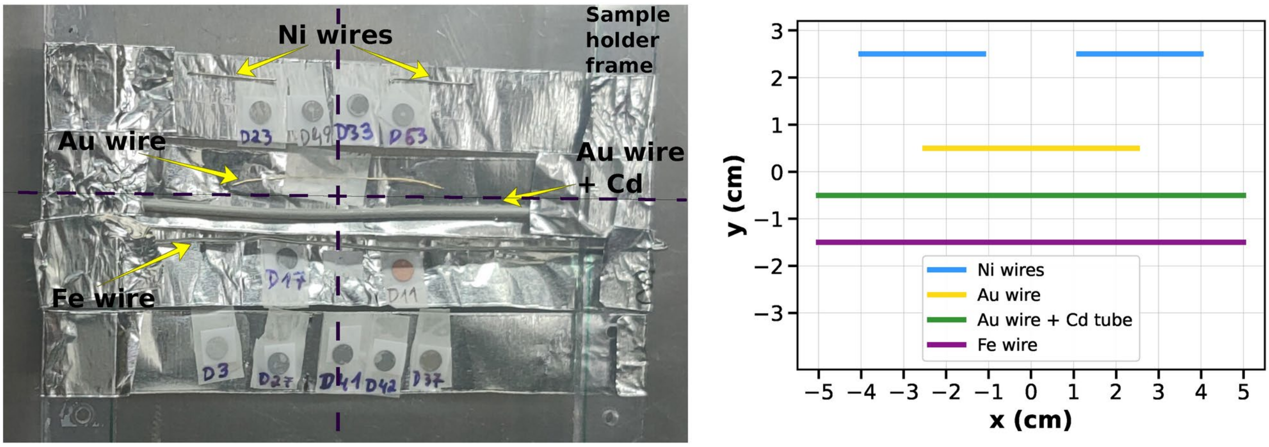


(a) (b)

**Fig. 5**. Example of (**a**) the activation foils and wires experimental setup for NAA and thermal neutron flux measurements and (**b**) their schematic positional configuration. The central *x* and *y* axes are marked with dashed lines and yellow arrows indicate the gold wires.

dimensions, calculating the percentage difference in the normalised neutron fluence at each data point ($\Delta\Phi$), and uniformity indexes (UI) across the centre of the field ($I > 70\%$), for both datasets, calculated as follows[21]:

$$UI = 1 - \frac{(\Phi_{max} - \Phi_{min})}{(\Phi_{max} + \Phi_{min})} \tag{2}$$

where $\Phi_{max}$ and $\Phi_{max}$ are the maximum and minimum normalised thermal neutron fluences, respectively.

## Absolute in-beam neutron activation analysis

We have selected 11 materials (one in two configurations) for the NAA based on the predicted Dingo neutron spectrum characteristics, which include gold and Mn(80%)-Ni(20%) alloy sensitive to thermal and epithermal neutron band; copper, erbium, gold + Cd, molybdenum, ruthenium and zirconium to epithermal/resonance region, and aluminium, indium, iron and nickel sensitive to fast neutrons; cross-sections of the reactions of interest are presented in Fig. 7. The characteristic $\gamma$-rays for all activated samples were measured individually using an HPGe detector, so that the main selection criteria included the reaction cross-section, $\gamma$ energy and branching ratio, half-life, price and availability or possibility of manufacturing. These materials are high purity (> 99.99%), naturally abundant 5 mm diameter and 0.5 mm thick discs, supplied by Advanced Engineering Materials (AEM), China. The gold discs were supplied by Goodfellow, UK and were approximately of 6 mm diameter and 0.025 mm thickness. We attached the foils to the preirradiated radiochromic films, relative to the centre of the beam, as shown in Fig. 8. The signals measured with the multifoil NAA technique have to be deconvolved to obtain the neutron spectrum estimate, which does not provide a unique solution. However, in this work, NAA was utilised to optimise the neutron spectrum in the Monte Carlo model by adjusting the neutron spectra relative to the decay-corrected simulated and experimental specific activities of each material.

In the simulation, the materials have been exposed to a $1\ \text{cm} \times 1\ \text{cm}$ beam and $n = 1 \times 10^9$ neutrons. The particles were generated 1 cm from the discs, using the neutron spectra predicted in the previous work[7] as the starting point. Characteristic $\gamma$-rays were scored as they entered an air-filled sphere surrounding the foil.

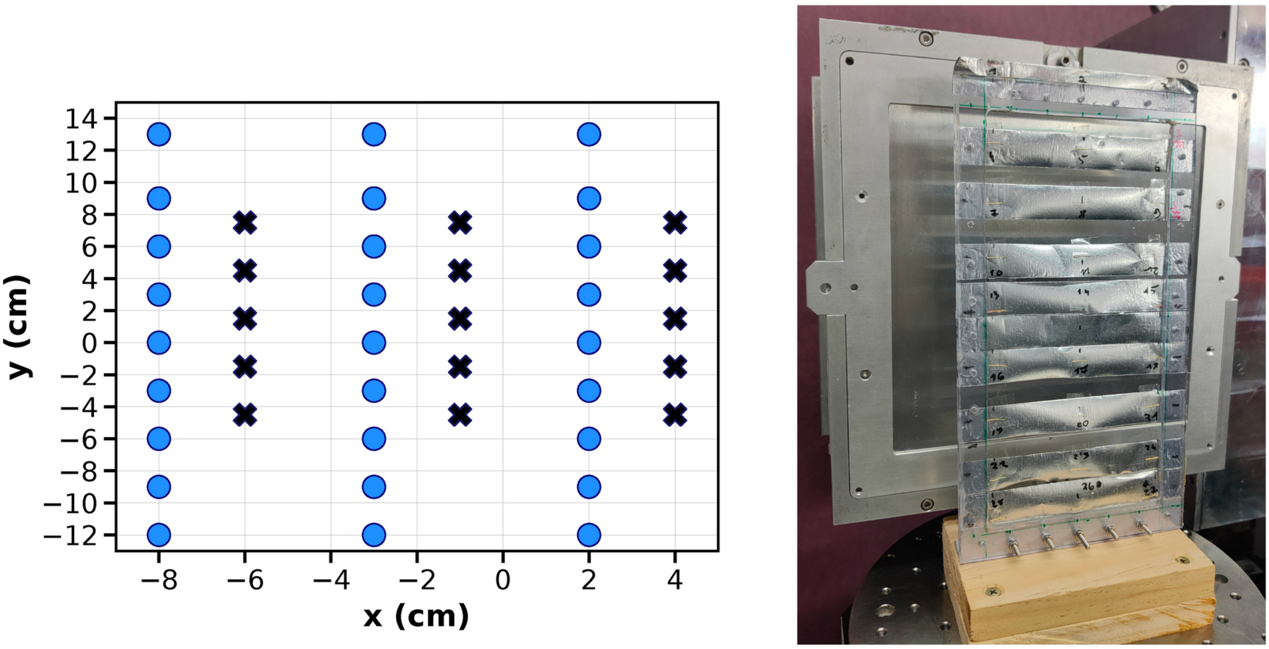


(a) (b)

**Fig. 6**. Illustration of the setup of gold activation wires relative to the centre of the field—(**a**) setup schematics, where black "X" and blue circles denote the positions at location A and B, respectively; and (**b**) picture of the experimental gold wire setup at location B.

Daughter isotopes were produced instantaneously and a decay correction was applied, also taking into account their depletion during the exposure. This is particularly important for materials that have half-lives shorter than the irradiation time.

Finally, we calculated the specific activities for the experimental data and the percentage change between the results for each material. The thermal and epithermal neutron component in the input spectrum was iteratively adjusted until the agreement for the bare and cadmium-covered gold discs was within 5% without compromising the acceptance conditions for neutron transmission through the sapphire crystal. Then, the resonance and fast neutron components were modified to maximise the agreement for the rest of the explored materials. Lastly, we simulated the refined in-beam neutron spectrum at location B (sample stage) with and without the sapphire filter.

### Absolute out-of-beam bonner sphere spectroscopy

The optimised neutron spectrum was validated against the pilot Bonner sphere spectroscopic data presented in the previous work, where we used the 8 locations parallel to the central beam axis depicted in Fig. 1, and a $^{6}$LiI scintillation detector—either bare or covered with 2", 3", 5", 8", 10" and 12" spherical high-density polyethylene moderators (HDPE). Each configuration was irradiated three times for 5 min using the $20\ \mathrm{cm} \times 20\ \mathrm{cm}$ high-intensity beam.

In the simulation, we scored the kinetic energy of neutrons entering a 12" spherical volume filled with air relative to the experimental Bonner spheres' positions. The results were then fed into the unfolding code as initial guess spectra to determine whether the simulated solution can produce the experimental counts, and limit the neutron energy range to a cut-off around 13.7 MeV for thermal neutron reactors. These were unfolded using the SpecUnPy App[22,23], SPUNIT algorithm, and the LiI response matrix, provided by[24], which consists of 221 bins and extends from $1 \times 10^{-9}$ to 100 MeV. The selected response matrix does not include the cadmium-covered detector. However, it provides a more detailed neutron energy distribution in contrast to the 31 energy intervals for the UTA4 response matrix. The maximum number of iterations in SpecUnPy was set to 1000, while the root mean square error (RMSE) for the experimental counts was estimated to be 10%. The general response matrix uncertainty is 3%, and the neutron spectra were unfolded with a maximum 10% RMSE. To validate the simulation results, we plotted the initial guess (simulated) and unfolded spectra on a logarithmic scale and normalised to unit lethargy and unit fluence to directly compare the shape of the spectra. The results were further normalised in two dimensions to the ratio between the thermal neutron peak in-beam to the one at each location out-of-beam. Finally, we calculate and plot logarithmic ratios ($\log_{10}(\Phi_{sim}/\Phi_{exp})$) for each energy bin. Additionally, we tabulated the number of iterations needed to calculate the solution, experimental counts and unfolded spectra RMSEs as well as the average logarithmic ratios in the thermal, epithermal and fast neutron windows and full energy range.

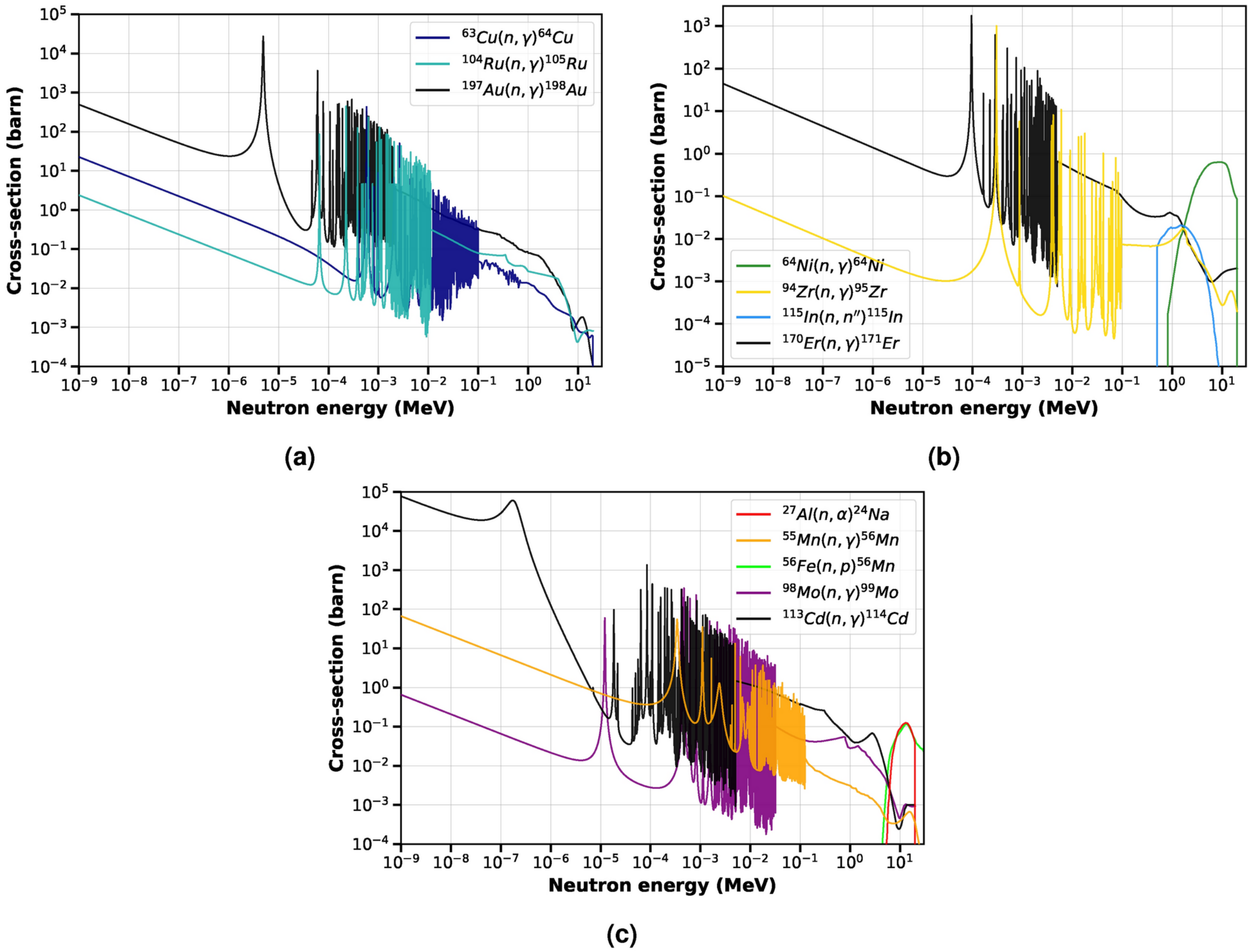


**Fig. 7**. Cross-sections of the selected nuclear reactions for NAA, and of the neutron capture in $^{113}$Cd, which was used as a thermal neutron filter.

## Results

### Validation of the neutron planar distribution

The simulated, normalised in two dimensions, $y$-axis line-profiles of the beam at locations A and B, compared to the relative neutron planar distribution measured with gold wires, are presented in Figs. 9 and 10, respectively. The percentage of changes between the simulated and experimental data points for both locations are shown in Tables 2 and 3. Beam's spatial characteristics, i.e. position of the centre of the neutron source and dispersion parameters, were iteratively adjusted in the model until the data points at the centre of the line-profiles were within 5% of the experimental results, and a reasonable agreement was found at the penumbra and of the field regions.

### Validation of the in-beam neutron spectrum

Table 4 lists the half-lives of the considered isotopes, their characteristic $\gamma$-ray energies, and the percentage change in the specific activities for the experimental and simulation results. The latter were normalised to the experimental neutron fluxes. The fast neutron component at Dingo above a few MeV is minimal, which combined with reaction cross-sections below 1 barn, led to very low count-rates for aluminium, indium, iron and nickel discs. All materials are therefore excluded from Table 4. In fact, indium features a high thermal neutron capture cross-section with a half-life of 54.2 min. However, in this work, we explored the isomeric transition reaction—$^{115}$In(n,n')$^{115m}$In, which reaches 0.02 barns at its peak around 1.5 MeV.

The optimised neutron spectrum at Dingo without any filter and with the sapphire filter in-beam is shown in Fig. 11. The results are normalised to the experimental neutron flux and per unit lethargy. The unfiltered neutron beam at Dingo consists of approximately 58.6% thermal, 21.2% epithermal and 20.2% fast neutrons. The sapphire filter decreases the neutron flux by approximately 45%, but effectively modifies the spectrum, providing a beam of around 97.7% thermal neutrons.

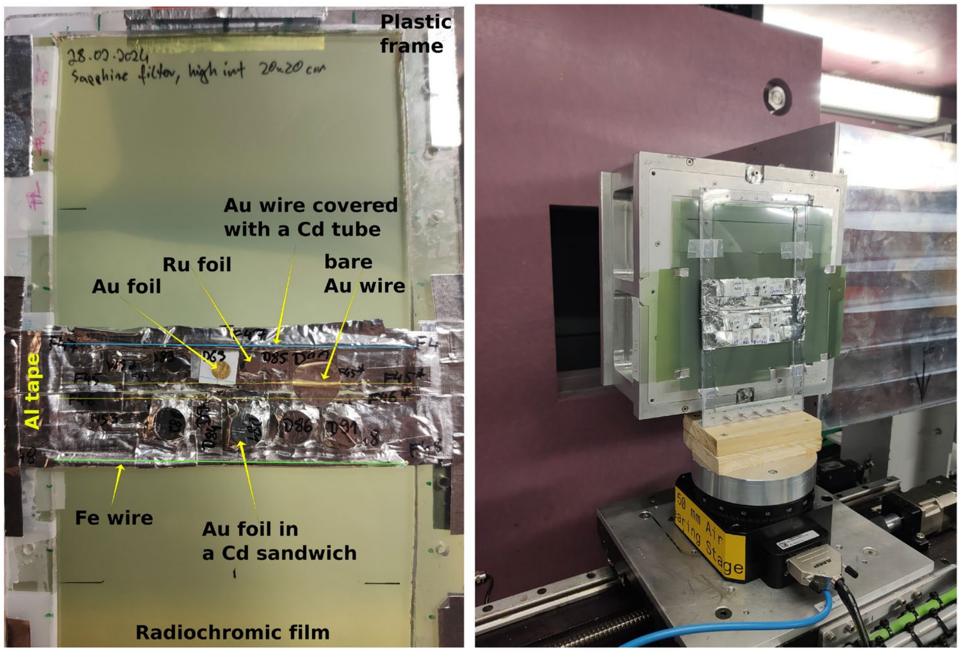


(a) (b)

**Fig. 8**. Example of (**a**) the sample holder with attached NAA samples (foils and wires) and a radiochromic film attached to the back for the relative beam position imaging, and (**b**) setup of the sample holder on the sample stage. Au, Au+Cd, and Fe wires shown in a) are around 10 cm and for clarity are additionally marked with thin yellow, blue, and green lines, respectively.

## Validation of the simulated out-of-beam neutron spectra

The simulated (initial guess) and unfolded spectra, and the logarithmic simulation to experiment ratios for the individual bins are illustrated in Fig. 12. The results are normalised per unit of lethargy and unit of fluence. The summary of the validation of the simulated and experimental out-of-beam neutron spectra are presented in Table 5.

Comparison of the simulated (initial guess) and unfolded out-of-beam neutron spectra, including the number of iterations needed to complete the calculation, counts and spectra RMSE and the average logarithmic ratios in the thermal, epithermal and fast neutron energy bands.

## Discussion

The Monte Carlo model developed for the Australian Center for Neutron Scattering (ACNS) Dingo beamline has been further refined to improve the accuracy of the predicted neutron spectrum in-beam and out-of-beam.

First, we measured the absolute neutron flux at the tertiary shutter wall exit (location A) using bare and cadmium-covered gold wires in both configurations—with and without the sapphire filter in the beam. When the latter is in use, we observed a decrease in the thermal/epithermal neutron flux of around 45%. Additionally, the beam at the Dingo beamline can also be filtered using a single or a double 0.7 mm thick cadmium sheet as a thermal neutron filter enclosed between two, approximately 1 mm thick, aluminium wafers. The cadmium filter is usually located between the pre-flight tube slits and the second flight tube, but can also be placed downstream at the nozzle, and decreases the total neutron flux by 90%. The thermal neutron flux for the unfiltered beam at location A is around $1.3\times10^{8}$ n/cm$^2$s, providing a beam intensity that is over 3 times higher than at location B. This is particularly advantageous for radiobiological research, where the dose rate is of great importance. Samples can be moved further upstream by another 50 cm, where the thermal neutron flux is around $2.75\times10^{8}$ n/cm$^2$s. The target neutron fluxes in clinical AB-BNCT are around $1\times10^{9}$ n/cm$^2$s. However, based on the neutron spectrum from Tsukuba University Hospital[25], only around 3.7% corresponds to the thermal neutron band. Dingo can provide over 5.5 brighter pure thermal neutron beam, opening up opportunities for a wide range of studies, particularly in radiobiology.

Next, we used sets of gold activation wires to study the neutron beam planar distribution and its dimensions at locations A and B. The neutron beam profiles at both locations exhibited slight but systematic non-uniformity, skewed toward negative values along the $x$- and positive along $y$-axes (Figs. 9 and 10). This non-uniformity is primarily caused by the vertical and horizontal offset of the reactor core relative to the beamline pinhole, a geometric effect that becomes more pronounced in the current 20 cm$\times$20 cm high-intensity mode, compared to our previous 10 cm$\times$10 cm high-resolution mode measurements, where the neutron distribution was effectively flat due to tighter collimation and smaller aperture size[7]. The systematic dip observed at $y = -3$ cm in Fig. 10 is likely due to neutron scattering from internal beamline structures not explicitly included in the current simulation geometry. Future refinements to the model will incorporate these factors to improve predictive

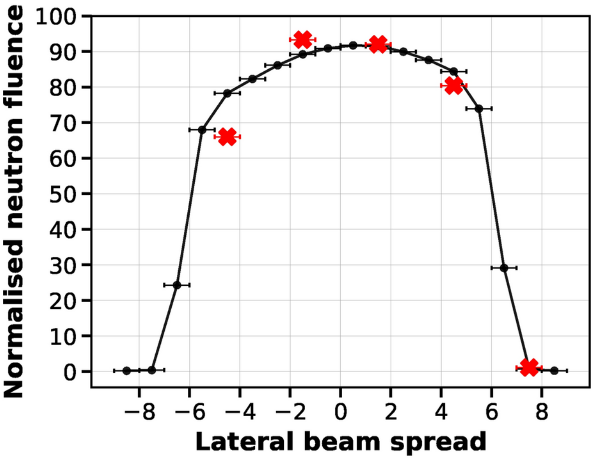


**(a)** Position 1

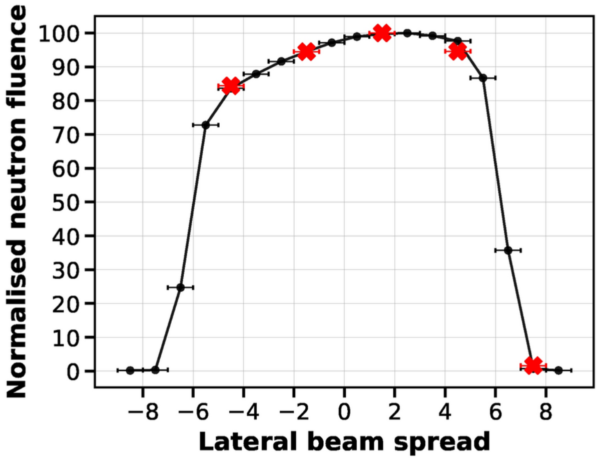


**(b)** Position 2

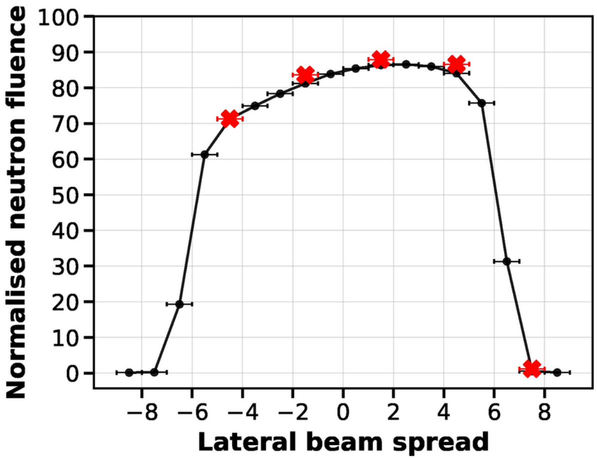


**(c)** Position 3

**Fig. 9**. Line-profiles along the $y$-axis at three positions of the simulated $20\ \mathrm{cm} \times 20\ \mathrm{cm}$ high-intensity neutron field at location A after 2D normalisation to the maximum gold activation wire specific activity (position 2—black line), compared to the experimental gold wire results (red "X"). Positions 1-3 correspond to the − 6 cm, − 1 cm and 4 cm black "X" positions of the line-profiles along $x$-axis in Fig. 6a. 95% confidence intervals for the simulated data, uncertainty in the experimental specific activities and positional uncertainty (horizontal error bars) are plotted; vertical error bars are very small and not clearly visible.

accuracy. On average, the simulated neutron beam profiles at locations A and B agreed within 2.3% and 2% of the gold wire readings in the beam centers, and within 6.5% and 24% in the penumbra, respectively (Tables 2 and 3). Larger discrepancies in the penumbra and out-of-field regions (up to 56% at location A and 95% at location B) were mainly due to positional uncertainty during sample placement, though these regions represent a small fraction of the total neutron flux (less than 2% at location A and 15% at location B). The sharp flux cut-off around $y = +12$ cm at location B is caused by neutrons scattering at the distal edge of the main field interacting with the inner edge of the third flight tube, which, along with the second flight tube, is positioned slightly lower than optimal; this effect is also captured in our model. The dimensions of the simulated beam ($I > 80\%$) were approximately 20 cm $\times$ 20 cm at location B and 11 cm $\times$ 11 cm upstream at location A.

The thermal component of the beam was modelled using the neutron transmission properties of the sapphire filter. The height of the thermal neutron peak, and the epithermal and fast neutron components were iteratively optimised using the experimental results of the NAA carried out with a set of 11 materials. These materials were selected based on their sensitivities to different neutron energy bands, with particular emphasis on the resonance region. Optimisation of the neutron spectrum against the experimental NAA results shall not compromise the achieved neutron transmission through the sapphire crystal, which depends solely on the energy distribution around the thermal neutron peak. The optimised neutron spectrum reached an agreement of 6% on average, highlighting the good accuracy of the model across the wide neutron energy band (Table 4). The agreement for the neutron beam filtered using a sapphire filter was within 13% on average with two outliers—molybdenum (26%) and erbium (35–48%). The results may depend on how Geant4 handles epithermal and fast neutron scattering in crystal structures. We observed a non-continuous distribution in the simulated in-beam neutron

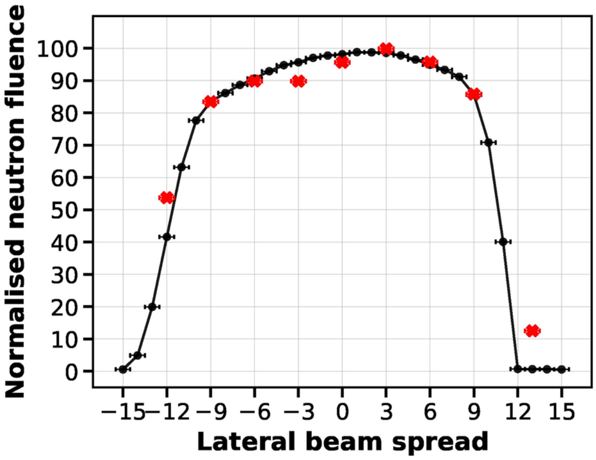


**(a)** Position 1

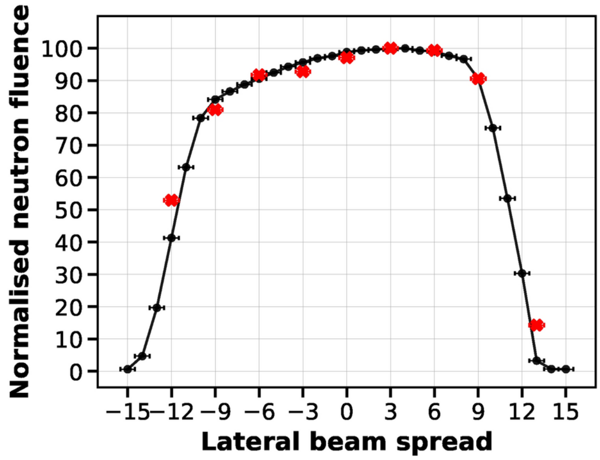


**(b)** Position 2

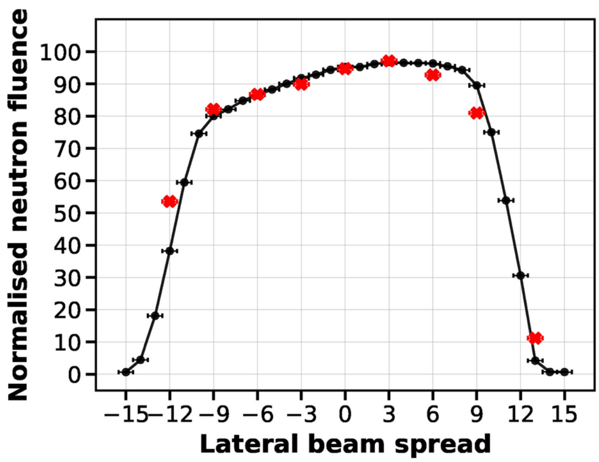


**(c)** Position 3

**Fig. 10**. Line-profiles along the $y$-axis at three positions of the simulated $20\ \mathrm{cm} \times 20\ \mathrm{cm}$ high-intensity neutron field at location B after 2D normalisation to the maximum gold activation wire specific activity (position 2—black line), compared to the experimental gold wire results (red "X"). Positions 1-3 correspond to the − 8 cm, − 3 cm and 2 cm blue circle positions of the line-profiles along $x$-axis in Fig. 6a. 95% confidence intervals for the simulated data, uncertainty in the experimental specific activities and positional uncertainty (horizontal error bars) are plotted; vertical error bars are very small and not clearly visible.

spectrum with the sapphire filter that corresponds to the resonance peaks of aluminium and its neutron capture cross-sections in the fast neutron region (Fig. 11). The reaction probability is higher due to the sapphire crystal thickness of 15 cm and can result in characteristic valleys in the resonance region that can overlap with resonance peaks for certain materials. To normalise the simulated activities, we used experimental neutron fluxes measured with 5 cm-long gold placed relative to the positions of the foils, determining the average beam intensities, and so, a few percent variations in the results presented in Table 4 are expected. Nonetheless, the proposed selection of NAA materials used in this study performed well, providing information on specific neutron energy windows although the fast neutron component at Dingo is too low for a conclusive evaluation of aluminium, indium, iron and nickel discs. The refined neutron spectrum consists of approximately 58.6% thermal, 21.2% epithermal and 20.2% fast neutrons, while the neutron beam filtered with a sapphire crystal constitutes around 97.7% thermal neutrons.

The out-of-beam neutron spectra were simulated using the refined in-beam neutron spectrum and used as the initial *guess spectrum* in the unfolding process to assess the agreement between the simulated and experimental solution. The maximum logarithmic ratio across all neutron energy windows and locations was within 0.6, with the maximum ratio for any individual bin also within 0.6, substantially improved compared to a ratio of 2 reported previously (Figure 8 in[7]). Average logarithmic ratios across all locations the thermal ($E_{th} < 0.4$ eV), epithermal (0.4 eV < $E_{epi}$ < 10 keV) and fast ($E_{fast}$ > 10 keV) neutron bands were within 0.27 ± 0.11, 0.01 ± 0.06 and 0.19 ± 0.13, respectively (Table 5). Typically, fewer than five iterations were sufficient for convergence, except at location 2, which required 15 iterations. The neutron spectrum RMSE was within 9.2% for location 1, 6.3% for location 2 and 5.2% for locations 3-8, resulting in a count RMSE of less than 10% on all cases. Unfolded spectra

| Position | *y*-axis position (cm) | ΔΦ(%) | Uniformity index (exp) | Uniformity index (sim) |
|---|---|---|---|---|
| 1 | − 4.5 ± 0.5★ | 18.5 ± 0.1 | 0.92 | 0.92 |
| | − 1.5 ± 0.5 | − 4.4 ± 0.1 | | |
| | 1.5 ± 0.5 | − 0.6 ± 0.1 | | |
| | 4.5 ± 0.5 | 4.9 ± 0.1 | | |
| | 7.5 ± 0.5■ | − 40.9 ± 0.8 | | |
| 2 | − 4.5 ± 0.5★ | − 0.9 ± 0.1 | 0.91 | 0.92 |
| | − 1.5 ± 0.5 | 0.0 ± 0.1 | | |
| | 1.5 ± 0.5 | − 0.2 ± 0.1 | | |
| | 4.5 ± 0.5 | 3.2 ± 0.1 | | |
| | 7.5 ± 0.5■ | − 56.3 ± 0.4 | | |
| 3 | − 4.5 ± 0.5★ | − 0.1 ± 0.1 | 0.90 | 0.90 |
| | − 1.5 ± 0.5 | − 2.9 ± 0.1 | | |
| | 1.5 ± 0.5 | − 1.8 ± 0.1 | | |
| | 4.5 ± 0.5 | − 2.9 ± 0.1 | | |
| | 7.5 ± 0.5■ | − 53.3 ± 0.5 | | |

**Table 2**. Percentage change between the simulated and experimental gold activation wires neutron fluence at Location A. Positions in the penumbra region along the *y*-axis are indicated with ★, while ■ denotes the locations out of beam with a total contribution to the neutron fluence below 2%.

| Position | *y*-axis position (cm) | ΔΦ(%) | Uniformity index (exp) | Uniformity index (sim) |
|---|---|---|---|---|
| 1 | − 12 ± 0.5★ | − 22.6 ± 0.2 | 0.92 | 0.91 |
| | − 9 ± 0.5 | 0.1 ± 0.2 | | |
| | − 6 ± 0.5 | 0.9 ± 0.2 | | |
| | − 3 ± 0.5 | 6.5 ± 0.3 | | |
| | 0 ± 0.5 | 2.6 ± 0.2 | | |
| | 3 ± 0.5 | − 1.3 ± 0.2 | | |
| | 6 ± 0.5 | − 0.9 ± 0.1 | | |
| | 9 ± 0.5 | − 0.1 ± 0.2 | | |
| | 13 ± 0.5★ | − 94.8 ± 0.2 | | |
| 2 | − 12 ± 0.5★ | − 22.0 ± 0.1 | 0.91 | 0.89 |
| | − 9 ± 0.5 | 3.9 ± 0.1 | | |
| | − 6 ± 0.5 | − 1.3 ± 0.1 | | |
| | − 3 ± 0.5 | 3.1 ± 0.2 | | |
| | 0 ± 0.5 | 1.8 ± 0.2 | | |
| | 3 ± 0.5 | − 0.1 ± 0.2 | | |
| | 6 ± 0.5 | − 0.3 ± 0.2 | | |
| | 9 ± 0.5 | 0.0 ± 0.2 | | |
| | 13 ± 0.5 ★ | − 77.0 ± 0.1 | | |
| 3 | − 12 ± 0.5★ | − 28.7 ± 0.2 | 0.91 | 0.92 |
| | − 9 ± 0.5 | − 2.6 ± 0.2 | | |
| | − 6 ± 0.5 | − 0.2 ± 0.2 | | |
| | − 3 ± 0.5 | 2.1 ± 0.2 | | |
| | 0 ± 0.5 | 0.5 ± 0.2 | | |
| | 3 ± 0.5 | − 0.3 ± 0.2 | | |
| | 6 ± 0.5 | 3.9 ± 0.2 | | |
| | 9 ± 0.5 | 10.5 ± 0.2 | | |
| | 13 ± 0.5★ | − 62.2 ± 0.3 | | |

**Table 3**. Percentage change between the simulated and experimental neutron fluence at location B; positions in the penumbra region along the *y*-axis are indicated with ★.

| Reaction | Half-life (h) | $\gamma$ energy (keV) | $\lvert \frac{A_{sim}-A_{exp}}{A_{exp}} \rvert$ (%) | |
|---|---|---|---|---|
| | | | No filter | $Al_2O_3$ |
| $^{197}Au(n,\gamma)^{198}Au$ | 65.2 | 411 | 0.2 ± 0.1% | 2.0 ± 0.1% |
| | | | 0.4 ± 0.1%■ | – |
| $^{63}Cu(n,\gamma)^{64}Cu$ | 12.7 | 1345.8 | 6.1 ± 0.8% | 3.0 ± 0.6% |
| $^{170}Er(n,\gamma)^{171}Er$ | 7.5 | 295.9 | 14.4 ± 0.3% | 47.6 ± 0.3% |
| | | 308.3 | 6.4 ± 0.2% | 34.6 ± 0.2% |
| $^{55}Mn(n,\gamma)^{56}Mn$ ★ | 2.6 | 846.8 | 1.5 ± 0.0% | 4.9 ± 0.0% |
| | | 1810.7 | 2.2 ± 0.1% | 2.4 ± 0.1% |
| $^{98}Mo(n,\gamma)^{99}Mo$ | 65.8 + 6.015 | 140.5 | 2.6 ± 0.6% | 26.0 ± 0.4% |
| $^{99}Mo \rightarrow {}^{99m}Tc + e^-$ | | | | |
| $^{58}Ni(n,p)^{58}Co$ | 1700.1 | 810.8 | 4.9 ± 2.1% | – |
| $^{104}Ru(n,\gamma)^{105}Ru$ | 4.44 | 724.3 | 6.0 ± 0.3% | 11.8 ± 0.5% |
| $^{94}Zr(n,\gamma)^{95}Zr$ | 1536.8 | 724.2 | 8.1 ± 2.0% | 4.2 ± 1.6% |
| | | 756.7 | 3.9 ± 2.0% | 6.0 ± 1.6% |

**Table 4**. NAA results—location A. For data points when more than one disc was used, an averaged result is presented. ■—discs covered with cadmium; ★—Mn 80% and Ni 20% alloy.

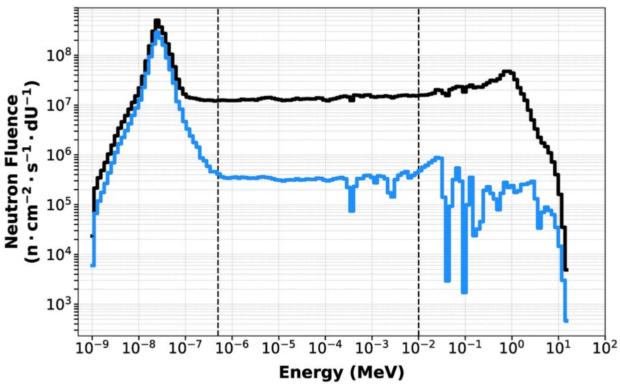


**Fig. 11**. Simulated neutron spectra at location B (sample stage) for the unfiltered beam (black) and with the sapphire filter in-beam (blue). 95% confidence intervals are plotted.

indicate a slightly higher thermal and a lower fast neutron component, at locations 1 and 2 (Fig. 12). The Bonner sphere measurement at location 4 was selected for validation, as it provides the most reliable reference point, positioned optimally (126 cm from the main beam axis and parallel to the primary beam), minimising positional and scattering uncertainties. Accurate validation at this position directly supports the reliability and predictive accuracy required for transitioning the current digital model towards a fully functional digital twin. Several factors may contribute to discrepancies observed in out-of-beam neutron scattering, including inaccuracies or omissions in the simulation geometry (e.g., unmodelled equipment in the sample room), variations in component material composition, detector response uncertainties, reactor operational fluctuations, and the presence or configuration of samples within the reactor core[7].

## Conclusion

In this work, we aimed to improve the accuracy of the predicted neutron spectrum by the Monte Carlo model of the Dingo beamline and extend its functionality by implementing a sapphire filter, and develop a user-friendly GUI. Neutron fluxes measured with and without the sapphire filter in-beam at the exit of the tertiary shutter wall (location A) were approximately 6.9 × $10^7$ n/cm$^2$s and 1.3 × $10^8$ n/cm$^2$s, respectively. The modelled sapphire crystal provides a beam of around 98% thermal neutrons, but decreases the thermal neutron flux by nearly 45%, which is in agreement with the experimental results. The simulated activation of 11 materials with varying sensitivities to thermal, epithermal and fast neutron energy windows, using the refined neutron spectrum, with and without the sapphire filter was on average within 13% and 5% of the experimental results, respectively. The predicted in-beam neutron spectrum consists of around 58.6% thermal, 21.2% epithermal and 20.2% fast neutrons. The average discrepancies between the simulated and experimental thermal neutron beam planar distribution at location A and location B (sample stage) are within 2.3% and 2% at the centre and 6% and 25% at the penumbra region, respectively. The average logarithmic ratios ($\log_{10}(\Phi_{sim}/\Phi_{exp})$) for thermal ($E_{th}$ < 0.4 eV), epithermal (0.4 eV < $E_{epi}$ < 10 keV) and fast ($E_{fast}$ > 10 keV) neutron energy windows were within

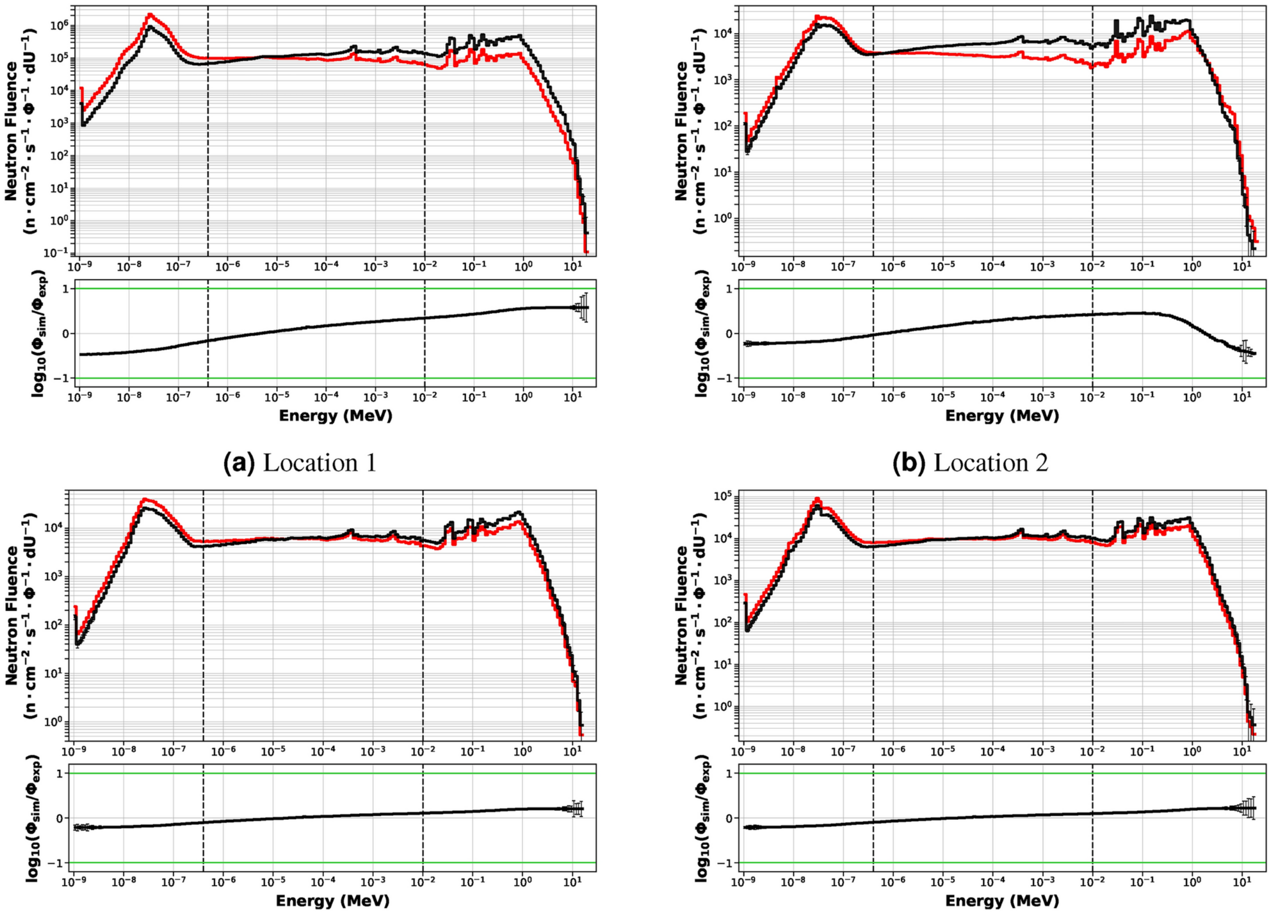


**(a)** Location 1 **(b)** Location 2 **(c)** Location 3 **(d)** Location 4

**Fig. 12**. Normalised simulated (black) and experimental (red) out-of-beam neutron fluence per unit lethargy (upper graphs) with corresponding logarithmic ratios (lower graphs) for all eight measurement locations (**a**–**h**). 95% confidence intervals for the simulated data are shown.

0.27 ± 0.11, 0.01 ± 0.06 and 0.19 ± 0.13, respectively. The neutron spectrum and counts RMSE were on average within 5.0 ± 1.4% and 9.1 ± 0.5%. Future work will focus on upgrading the GUI to integrate real-time beamline sensor data, and provide interactive visualisation, automated reporting and modular configuration capabilities. These improvements will enhance usability, enabling beamline optimisation tailored to specific experimental needs, and will support the development of novel neutron detection and imaging technologies.

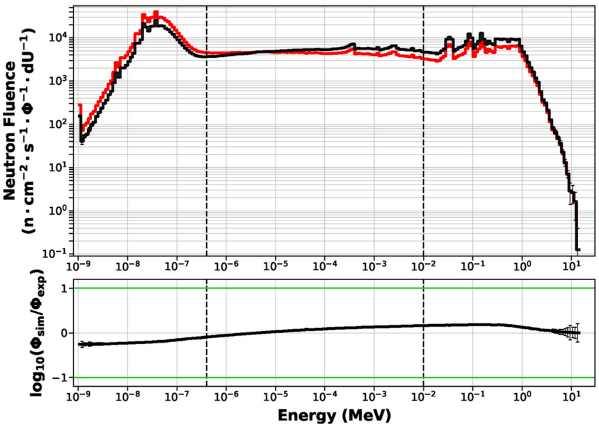


**(e)** Location 5

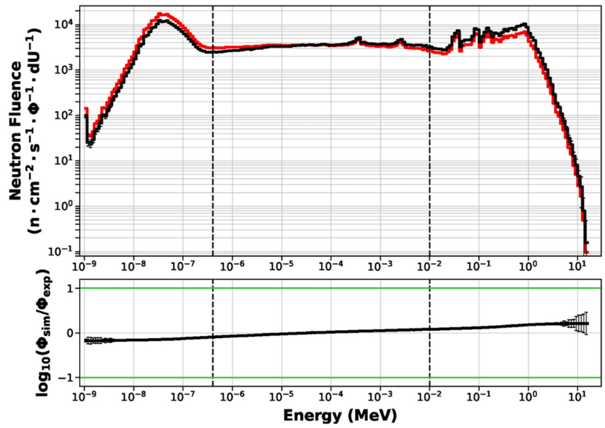


**(f)** Location 6

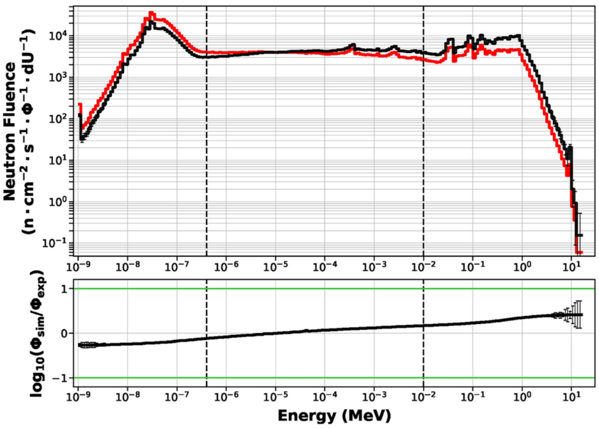


**(g)** Location 7

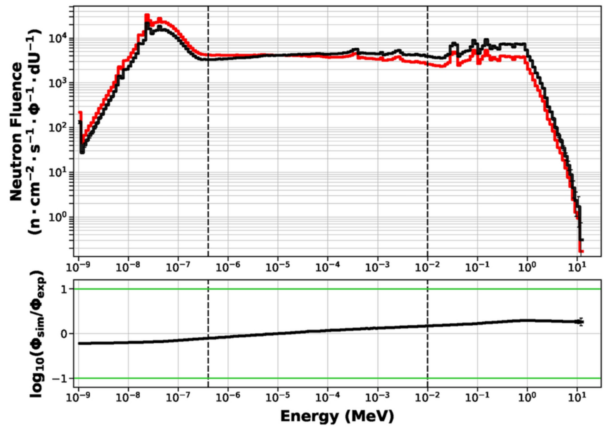


**(h)** Location 8

**Figure 12.** (continued)

| | | Counts | Spectrum | $\log_{10}(\overline{\Phi_{sim}}/\overline{\Phi_{exp}})$ | | | |
|---|---|---|---|---|---|---|---|
| Location | No. iterations | RMSE (%) | RMSE (%) | Thermal | Epithermal | Fast | Overall |
| 1 | 4 | 9.1 | 9.2 | − 0.4 | 0.0 | 0.5 | 0.1 |
| 2 | 15 | 10.0 | 6.3 | − 0.6 | − 0.2 | − 0.1 | − 0.2 |
| 3 | 2 | 9.4 | 3.9 | − 0.2 | 0.0 | 0.2 | 0.0 |
| 4 | 2 | 8.4 | 3.7 | − 0.2 | 0.0 | 0.2 | 0.0 |
| 5 | 5 | 9.7 | 4.5 | − 0.2 | 0.0 | 0.1 | 0.0 |
| 6 | 2 | 8.2 | 3.2 | − 0.2 | 0.0 | 0.1 | 0.0 |
| 7 | 3 | 9.0 | 5.2 | − 0.2 | 0.0 | 0.3 | 0.1 |
| 8 | 4 | 8.9 | 4.5 | − 0.2 | 0.0 | 0.2 | 0.0 |

**Table 5.** Comparison of the simulated (initial guess) and unfolded out-of-beam neutron spectra, including the number of iterations needed to complete the calculation, counts and spectra RMSE and the average logarithmic ratios in the thermal, epithermal and fast neutron energy bands.

## Data availability

All data generated or analysed during this study are included in this published article (and its Supplementary Information files) or are available from the corresponding author on reasonable request.

Received: 15 December 2024; Accepted: 26 March 2025
Published online: 02 April 2025

## References


1. Garbe, U. et al. A new neutron radiography/tomography/imaging station DINGO at OPAL. *Phys. Procedia* **69**, 27–32. https://doi.org/10.1016/j.phpro.2015.07.003 (2015).
2. Salvemini, F., Bevitt, J., Liss, K. D. & Garbe, U. DINGO—The neutron imaging station at ANSTO: Embracing material science, palaeontology, and cultural heritage. *Neutron News* **27**, 14–19. https://doi.org/10.1080/10448632.2016.1163982 (2016).
3. Stamatelatos, I. E. & Messoloras, S. Sapphire filter thickness optimization in neutron scattering instruments. *Rev. Sci. Instrum.* **71**, 70–73. https://doi.org/10.1063/1.1150163 (2000).
4. Adib, M., Kilany, M., Habib, N. & Fathallah, M. Neutron transmission of single-crystal sapphire filters. *Czechoslov. J. Phys.* **55**, 563–578. https://doi.org/10.1007/s10582-005-0061-7 (2005).
5. Mildner, D. F. R., Arif, M., Stone, C. A. & Crawford, R. K. The neutron transmission of single-crystal sapphire filters. *J. Appl. Crystallogr.* **26**, 438–447. https://doi.org/10.1107/s0021889893000433 (1993).
6. Gholamzadeh, Z. et al. Experimental evaluation of transition rate of sapphire crystal for thermal and fast neutrons using mnsr vertical neutron beam line. *Heliyon* **10**, e24160. https://doi.org/10.1016/j.heliyon.2024.e24160 (2024).
7. Jakubowski, K. et al. A Monte Carlo model of the Dingo thermal neutron imaging beamline. *Sci. Rep.* https://doi.org/10.1038/s41598-023-44035-4 (2023).
8. Sauerwein, W. A. et al. Principles, recent developmentsand perspectives in boron neutroncapture therapy (BNCT). *Bio-Algorithms Med-Syst.* **19**, 48–53. https://doi.org/10.5604/01.3001.0054.1824 (2023).
9. Sauerwein, W. A. G. et al. Hadron therapy in radiation oncology and why BNCT is a paradigm shift. *Health Technol.* https://doi.org/10.1007/s12553-024-00848-5 (2024).
10. Safavi-Naeini, M. et al. Opportunistic dose amplification for proton and carbon ion therapy via capture of internally generated thermal neutrons. *Sci. Rep.* https://doi.org/10.1038/s41598-018-34643-w (2018).
11. Howell, N. et al. Neutron capture enhances dose and reduces cancer cell viability in and out of beam during helium and carbon ion therapy. *Int. J. Radiat. Oncol. Biol. Phys.* https://doi.org/10.1016/j.ijrobp.2024.02.052 (2024).
12. Vagena, E., Theodorou, K. & Stoulos, S. Thick-foils activation technique for neutron spectrum unfolding with the MINUIT routine—Comparison with GEANT4 simulations. *Nucl. Instrum. Methods Phys. Res. Sect. A Accel. Spectrom. Detect. Assoc. Equip.* **887**, 64–69. https://doi.org/10.1016/j.nima.2018.01.025 (2018).
13. Stefanik, M. et al. Neutron field study of p(24)+ be source reaction using the multi-foil activation technique. *Fusion Eng. Des.* **146**, 2053–2056. https://doi.org/10.1016/j.fusengdes.2019.03.100 (2019).
14. Agostinelli, S. et al. Geant4—A simulation toolkit. *Nucl. Instrum. Methods Phys. Res. Sect. A Accel. Spectrom. Detect. Assoc. Equip.* **506**, 250–303. https://doi.org/10.1016/s0168-9002(03)01368-8 (2003).
15. Allison, J. et al. Geant4 developments and applications. *IEEE Trans. Nucl. Sci.* **53**, 270–278. https://doi.org/10.1109/tns.2006.869826 (2006).
16. Allison, J. et al. Recent developments in Geant4. *Nucl. Instrum. Methods Phys. Res. Sect. A Accel. Spectrom. Detect. Assoc. Equip.* **835**, 186–225. https://doi.org/10.1016/j.nima.2016.06.125 (2016).
17. Barton, J. Filters for thermal neutron radiography. *Nondestruct. Test. Eval.* **16**, 95–110. https://doi.org/10.1080/10589750108953067 (2001).
18. Cai, X.-X. & Kittelmann, T. NCrystal: A library for thermal neutron transport. *Comput. Phys. Commun.* **246**, 106851. https://doi.org/10.1016/j.cpc.2019.07.015 (2020).
19. Kittelmann, T. & Cai, X.-X. Elastic neutron scattering models for NCrystal. *Comput. Phys. Commun.* **267**, 108082. https://doi.org/10.1016/j.cpc.2021.108082 (2021).
20. Kittelmann, T. *NCrystal: A Library for Thermal Neutron Transport in Crystals and Other Materials*. https://github.com/mctools/ncrystal/wiki (2025).
21. Jackson, E. *et al.* Acceptance Testing and Quality Assurance Procedures for Magnetic Resonance Imaging Facilities. Tech. Rep. (AAPM, 2010). https://doi.org/10.37206/101.
22. Machado, I. A., García-Baonza, R. & de Sousa Lacerda, M. A. SpecUnPy: A python GUI/App for neutron spectrum unfolding. *Appl. Radiat. Isot.* **200**, 110974. https://doi.org/10.1016/j.apradiso.2023.110974 (2023).
23. Machado, I. A., García-Baonza, R., Vega-Carrillo, H. R. & de Sousa Lacerda, M. A. Stopping criteria for neutron spectrum unfolding algorithms. *Appl. Radiat. Isot.* **212**, 111456. https://doi.org/10.1016/j.apradiso.2024.111456 (2024).
24. Lacerda, M. et al. A new response matrix for $^{6}$LiI scintillator BSS system. *Nucl. Instrum. Methods Phys. Res. Sect. A Accel. Spectrom. Detect. Assoc. Equip.* **868**, 122–128. https://doi.org/10.1016/j.nima.2017.06.057 (2017).
25. Kumada, H. et al. Development of LINAC-based neutron source for boron neutron capture therapy in University of Tsukuba. *Plasma Fusion Res.* **13**, 2406006–2406006. https://doi.org/10.1585/pfr.13.2406006 (2018).


## Acknowledgements

This research was supported by the ANSTO Tesla high-performance computing cluster and the Australian Government's National Collaborative Research Infrastructure Strategy (NCRIS), with computational resources on Gadi provided through the National Computational Merit Allocation Scheme (NCMAS). The authors acknowledge the support of the University of Wollongong Matching Scholarship and the International Postgraduate Tuition Award, and the Australian Institute of Nuclear Science and Engineering (AINSE) Residential Student Scholarship (RSS). The authors wish to acknowledge Associate Professor Marco Aurélio de Sousa Lacerda for sharing their enhanced response matrix that was used to unfold the Bonner Sphere measurements and Mr Igor Machado for his assistance with the use of SpecUnPy.

## Author contributions

K.B. developed and implemented the simulation model, designed and conducted all simulation, experimental and analysis work described in this paper, and prepared the manuscript. M. SN. established this project and contributed extensively to the theoretical and analytic, and performed the experimental measurements. J.J.B. and U.G. facilitated access to the Dingo beamline, oversaw the experimental preparation and execution, provided technical and scientific advice, and contributed to manuscript preparation. S.O. provided all technical drawings, geometries and material compositions essential for implementation of the simulation model and assisted with the interpretation of results. A.S. performed measurements of activated samples using the HPGe detector, contributed to data analysis and interpretation, assisted with manuscript preparation and provided scientific advice. D.R.F. provided technical guidance and contributed to the manuscript preparation. N.H., C.D. and F.S. participated in the experimental work and manuscript preparation. A.R., L.T.T., and S.G. provided guidance on theoretical development and simulation methodology. All authors reviewed the manuscript.

## Declarations

### Competing interests
The authors declare no competing interests.

### Additional information
**Supplementary Information** The online version contains supplementary material available at https://doi.org/10.1038/s41598-025-96164-7.

**Correspondence** and requests for materials should be addressed to M.S.-N.

**Reprints and permissions information** is available at www.nature.com/reprints.

**Publisher's note** Springer Nature remains neutral with regard to jurisdictional claims in published maps and institutional affiliations.